

Assessment of Physical Parameterizations Using a Global Climate Model with Stretchable Grid and Nudging

O. COINDREAU

Commisariat à l'Énergie Atomique, Bruyères-le-Châtel, France

F. HOURDIN, M. HAEFFELIN, A. MATHIEU, AND C. RIO

Laboratoire de Météorologie Dynamique, CNRS, IPSL, Paris, France

(Manuscript received 19 October 2005, in final form 16 May 2006)

ABSTRACT

The Laboratoire de Météorologie Dynamique atmospheric general circulation model with zooming capability (LMDZ) has been used in a nudged mode to enable comparison of model outputs with routine observations and evaluate the model physical parameterizations. Simulations have been conducted with a stretched grid refined over the vicinity of Paris, France, where observations, collected at the Trappes station (Météo-France) and at the Site Instrumental de Recherche par Télédétection Atmosphérique observatory, are available. For the purpose of evaluation of physical parameterizations, the large-scale component of the modeled circulation is adjusted toward ECMWF analyses outside the zoomed area only, whereas the inside region can evolve freely. A series of sensitivity experiments have been performed with different parameterizations of land surface and boundary layer processes. Compared with previous versions of the LMDZ model, a “thermal plume model,” in association with a constant resistance to evaporation improves agreement with observations. The new parameterization significantly improves the representation of seasonal and diurnal cycles of near-surface meteorology, the day-to-day variability of planetary boundary layer height, and the cloud radiative forcing. This study emphasizes the potential of using a climate model with a nudging and zooming capability to assess model physical parameterizations.

1. Introduction

The skill of atmospheric general circulation models (GCMs) relies, to a large part, on the representation of subgrid-scale atmospheric processes such as turbulent mixing in the planetary boundary layer (PBL), cumulus and dry convection, and surface thermodynamics. Those processes can only be represented statistically in the models through so-called parameterizations. In the frame of climate change projections, those parameterizations must, as much as possible, rely on physics and not be tied to reproducing current observations. Improvement and validation of those parameterizations is a constant effort in climate modeling groups. Different strategies have been developed. In the first approach, model changes are directly assessed in the full 3D climate model by comparing simulations and observations

(or meteorological analysis) in terms of statistics (means, standard deviations, correlations, etc.). This approach is at the basis of intercomparison programs such as the Atmospheric Model Intercomparison Project (Gates 1992). This approach is important because one validates at once the whole set of physical parameterizations coupled to large-scale dynamics. The disadvantage is that it is often difficult to separate which of the parameterizations (or combination of them) is responsible for a discrepancy between observations and model.

To overcome this difficulty, a second approach was developed in the last two decades that consists of comparing single-column versions of the set (or a subset) of physical parameterizations with results of explicit simulations of the same phenomenon, using the so-called cloud resolving models (Guichard et al. 2004) or large eddy simulations (LESs; Ayotte et al. 1996; Lenderink et al. 2004). This approach contributed to improving the description of some phenomenon and has led to important international programs such as the European

Corresponding author address: Dr. Olivia Coindreau, CEA, DASE/LDG/SEG, BP 12, 91 680 Bruyères-le-Châtel, France.
E-mail: olivia_coindreau@yahoo.fr

Cloud-Resolving Modeling Project, the European Cloud Systems research project, and the Global Energy and Water Cycle Experiment Cloud System Study. With this approach, it is possible to extract a number of diagnostics from the explicit simulations. It is also easier to identify which component of the parameterization is correct. The disadvantage here is that the explicit simulations are quite computationally demanding and the number of cases limited.

A complementary approach consists of comparing continuous simulations of the local meteorology, relying for the large-scale forcing on the operational meteorological analyses, with routine observations collected at advanced atmospheric profiling observatories. For instance, Morcrette (2002) assesses the European Centre for Medium-Range Weather Forecasts (ECMWF) model cloudiness and surface radiation by direct comparisons with data from the Atmospheric Radiation Measurement (ARM) program (Ackerman and Stokes 2003) over a period of 1 month. The meteorological analysis can also be used to define the boundary conditions of a limited-area model. For instance, Guichard et al. (2003) make use of the ARM data for directly evaluating the predictions and parameterizations of the fifth-generation Pennsylvania State University–National Center for Atmospheric Research Mesoscale Model (MM5), and Chiriaco et al. (2006) use data from the Site Instrumental de Recherche par Télédétection Atmosphérique (SIRTA) observatory (Haefelin et al. 2005) to assess cloud physics parameterizations in the MM5. Ghan et al. (1999) compared and evaluated the prospects and limitations of these different approaches in evaluating the physical parameterizations. We present here a tool that can be classified in the third category. The Laboratoire de Météorologie Dynamique GCM with zooming capability (LMDZ), an atmospheric GCM involved recently in the production of climate change simulations for the next Intergovernmental Panel on Climate Change report (Marti et al. 2005), is used in a nudged mode. The model is forced to stay close to the synoptic situation by relaxing the large-scale circulation toward the meteorological analyses. This nudging technique is well known in the community of transport modelers and can be presented as a poor version of data assimilation (Jeuken et al. 1996). Here, real observations are replaced by the results of a former assimilation procedure performed in meteorological centers.

The first focus of this paper is to show the potential of this approach for model development and validation. This is illustrated with a series of sensitivity experiments performed with the LMDZ model. In the present study, a zooming capability of the GCM is used that allows the grid to be refined around a site where rou-

tine observations are available. For the purpose of evaluating the physical parameterizations, the large-scale component of the modeled circulation is adjusted toward ECMWF analyses outside the zoomed area only, whereas the inside region can evolve freely. The outputs of the LMDZ model zoomed over the Paris area are compared with observations of the SIRTA observatory. It is shown in particular that despite nudging, model results are highly sensitive to the parameterization of boundary layer and surface processes.

The second focus of this paper is to test in a real 3D context the “thermal plume model” (th) developed to account for nonlocal transport by mesoscale thermal cells in the convective boundary layer (Hourdin et al. 2002). The influence of the PBL parameterization is evaluated by running the model in the configuration previously described and confronting model outputs with SIRTA observations. It allows the new thermal plume model to be compared with the standard PBL parameterization of the LMDZ model.

In section 2, a description is made of the model and its physical parameterizations. The nudging technique is also briefly described and results of the reference experiment are compared with ECMWF analyses. Observed meteorological data collected at the Trappes station (Météo-France), such as temperature and relative humidity, are used to assess the sensitivity of the model to the parameterization of the land surface (section 3) and boundary layer (section 4) schemes. Comparisons are performed during the period January 2000–December 2003. Observations of the convective PBL realized at SIRTA in May–June 2004 during an intensive observation period are compared in the last section with the results obtained with the best set of physical parameterizations.

2. Description of the model and observations

a. The LMDZ GCM

The GCM used in this study is based on a finite-difference formulation of the primitive equations of meteorology, first described by Sadourny and Laval (1984). The dynamical equations are discretized on a longitude–latitude Arakawa C-grid (Kasahara 1977) with zooming capability. Discretization in the vertical is done by using a hybrid σ – p coordinate system (Simmons and Burridge 1981) with 19 levels.

The physical package of the version used here is described in detail by Hourdin et al. (2006). The radiative transfer model is a refined version of the scheme developed by Fouquart and Bonnel (1980) for the solar part, and the terrestrial part is based on Morcrette et al.

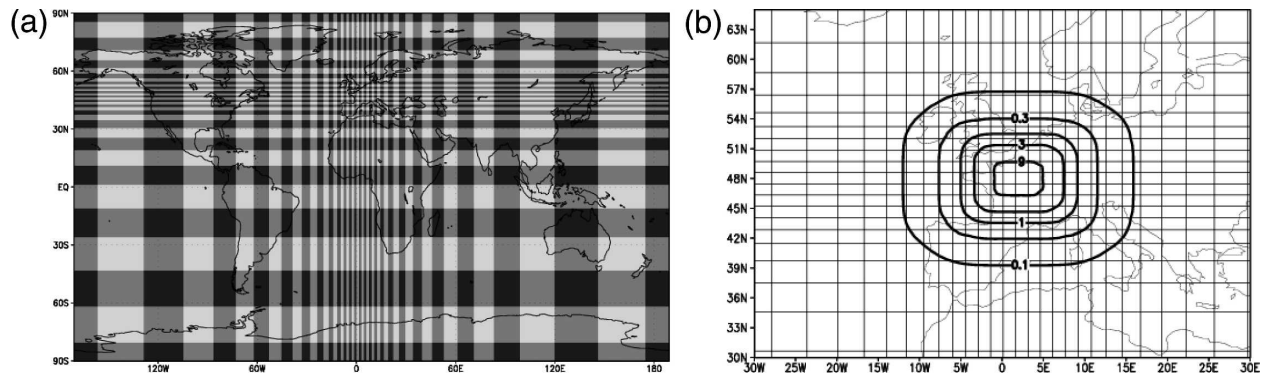


FIG. 1. (a) LMDZ stretched grid with 48×32 points. (b) A zoom over Europe showing the nudging time constant. Contour levels are 0.1, 0.3, 1, 3, and 9 days. The time constant is a maximum at the center of the zoomed area and decreases as the grid resolution decreases.

(1986). Turbulent mixing in the PBL is parameterized by using a classical local closure with a turbulent coefficient that depends on the vertical shear of the horizontal wind and on the local Richardson number following Laval et al. (1981). A countergradient term for potential temperature is introduced to allow upward heat transport in a neutral or slightly stable atmosphere as is frequently observed in the convective PBL (Dearhoff 1972). Condensation is parameterized separately for convective and nonconvective clouds. Moist convection is accounted for with the Emanuel (1991) mass flux scheme. Large-scale condensation and cloud cover for both large-scale and convective clouds is prescribed through a probability distribution function of the sub-grid-scale total water following Bony and Emanuel (2001). The large-scale transport of vapor and condensed water is computed with the finite-volume scheme of Van Leer (1977).

The standard parameterization scheme for land surface processes in LMDZ is the Schématisation des Echanges Hydriques à l'Interface Biosphère-Atmosphère (SECHIBA; Ducoudré et al. 1993; De Rosnay and Polcher 1998; Ducharne and Laval 2000) recently used in the dynamical vegetation model Organizing Carbon and Hydrology in Dynamic Ecosystems (ORCHIDEE; Krinner et al. 2005). SECHIBA is a parameterization of the hydrological exchanges between the land surface and the atmosphere. There are two moisture reservoirs of water in the soil: a superficial one, created as soon as precipitation is larger than evaporation, and a lower one. As long as the superficial reservoir exists, the water content of the lower reservoir can only increase by drainage between the two soil layers. When no upper reservoir exists, the deep one works as a simple bucket (Manabe 1969). The total depth of the soil is 2 m and its maximum water content is 300 mm. The grid box is subdivided into several land

tiles, each corresponding to one hydrological soil column. Water exchanges between columns are allowed in the lower layer. Vegetation types are characterized by their root density distributions, their leaf area index, and their canopy resistance. In the region studied here (whose area is $120 \times 120 \text{ km}^2$), the land surface is composed of cultures (0.71), bare soil (0.24), deciduous forest (0.04), and grassland (0.01). Thermal conduction below the surface is computed with an 11-layer model following Hourdin et al. (1993).

b. Model configuration

To assess physical parameterizations of the model over a given area, the model is run with its zooming capability in a nudged mode. The region studied here is the vicinity of Paris, France. At the center of the zoom, fixed at 48°N , 2°E , the resolution reaches about 120 km (see Fig. 1a). The small number of grid points (48×32) allows a series of pluriannual simulations to be performed even on a standard personal computer with a mesh size that is typical of state-of-the-art climate models.

Meteorological fields (wind, temperature, and humidity) are relaxed toward analyzed fields of the ECMWF, by adding a nonphysical relaxation term to the model equations:

$$\frac{\partial X}{\partial t} = F(X) + \frac{X^a - X}{\tau}, \quad (1)$$

where X represents any meteorological field, F is the operator describing the dynamical and physical processes that determine the evolution of X , X^a is the analyzed field of ECMWF, and τ is the time constant. The choice of the right value of τ is crucial as it determines the effect of the observations on the solution. As suggested by Hoke and Anthes (1976), the optimal value

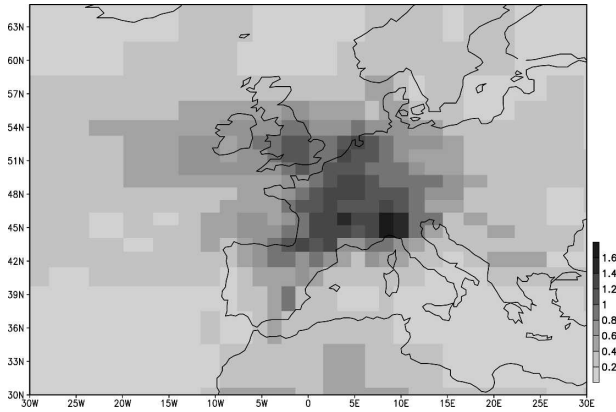


FIG. 2. Root-mean-square difference between simulated temperatures and analyses (in the second model layer) in January 1998. Large differences are observed at the center of the zoomed area, showing that a certain degree of freedom is left to parameterizations. Away from the zoomed area, differences are small, indicating that the large-scale component of the modeled circulation is adjusted toward ECMWF analyses.

should depend on the observational accuracy, the kind of variable being adjusted, and the typical magnitude of the model forcing. In the LMDZ model, τ can be chosen differently for each variable and each region.

Before applying relaxation, ECMWF data are interpolated on the stretched grid of the LMDZ model. The time constant in Eq. (1) varies from 30 min outside the zoomed area to 10 days inside for temperature and wind fields (see Fig. 1b). Humidity fields are relaxed with a larger time constant outside the zoomed area (5 h). With these values of the relaxation coefficient, the large-scale component of the modeled circulation is adjusted toward ECMWF analyses whereas the evolution of meteorological fields in the zoomed area is conditioned by physical parameterizations of the model. As shown in Fig. 2, simulated temperatures are close to analyses away from the center of the zoomed area, indicating a strong forcing of the synoptic situation. On the contrary, simulated temperatures and analyses are

quite different at the center of the zoomed area, showing that a certain degree of freedom is left to parameterizations.

A series of experiments, differing by their land surface and boundary layer schemes, are carried out for the period January 1998–June 2004 [the last period, running from May to June 2004, corresponding to the water vapor profiling intercomparison campaign (VAPIC) described below]. One year is needed to reach a regime state for the seasonal cycle of surface hydrology (which is not initialized with observations). In the analysis presented hereafter, evaluations are made on the period January 2000–June 2004, skipping the first two years. The time step for large-scale dynamics is 1.5 min whereas most model physics are calculated every 30 min. The model variables we analyze are those of the grid box containing the point 48°N, 2°E.

c. Observations

Model variables such as temperature, relative humidity, soil moisture, evaporation, and precipitation rate, PBL height, and downward shortwave fluxes are investigated and compared with measurements. Those measurements are listed in Table 1.

For comparisons of standard meteorological parameters such as temperature, humidity, and precipitation, over long time periods, we used hourly data provided by the meteorological center of Trappes (48.8°N, 2.0°E), France, operated by Météo-France. This station, located 30 km southwest of Paris, provided hourly values of the standard parameters for the period January 2000–December 2003.

For comparison of physical and radiative properties, we use the measurement synergies provided by the SIRTA observatory, located in Palaiseau (48.7°N, 2.2°E), France, 25 km south of Paris. SIRTA gathers a suite of active (lidar and radar) and passive (radiometers) remote sensing instruments and in situ sensors to describe atmospheric processes in the atmospheric boundary layer and the free troposphere (Haefelin et

TABLE 1. List of available observations.

Location	Period	Sensors	Geophysical parameters
Trappes	Jan 2000–Dec 2003	Standard weather sensors 2 m above ground	Temperature, humidity, and precipitation
SIRTA	May 2004–Jun 2004	Standard weather sensors 15 m above ground	Temperature, humidity, and precipitation
		Radiometric station (BSRN standard) RS90 and RS92 radiosondes	Downwelling direct, diffuse, and global solar irradiance Vertical profiles of temperature, pressure, humidity, and horizontal wind; boundary layer height
		Backscattering lidar	Boundary layer height

al. 2005). For our study, we focus on an intensive observation period associated with VAPIC that took place at SIRTa from 18 May to 17 June 2004. During this period SIRTa measurements were enhanced both in terms of sensors and operation hours with both day and night measurements. Fifty Vaisala RS92 radiosondes were launched from the SIRTa site in addition to the Vaisala RS90 radiosondes launched from Trappes at the standard 0000 and 1200 UTC as part of the Météo-France operational radiosonde network. Vertical profiles of thermodynamic properties measured by radiosondes were used to derive the PBL height. The SIRTa multichannel backscattering lidar for cloud and aerosol research was operated on 20 different days during VAPIC. The lidar data were analyzed to retrieve the diurnal cycle of the PBL height on those days. Direct, diffuse, and global components of the downwelling solar irradiance are measured at SIRTa according to protocols recommended by the Baseline Surface Radiation Network (Ohmura et al. 1998). The two measurement sites are expected to be representative of a wide surrounding area, which is relatively flat, with an homogeneous land surface divided in agricultural fields, housing and industrial developments, and wooded areas. During the VAPIC intensive observation period, hourly observations of relative humidity and temperature fields made by the meteorological center of Trappes are found to be consistent with SIRTa measurements. Thus, the spatial variability of temperature and humidity is relatively weak and its influence on 2000–03 monthly normals is deemed negligible. Precipitation has a larger spatial variability, and the average monthly data of five meteorological stations, operated by Météo-France and located inside the grid cell of the model considered here, have been used to check the representativity of the Trappes station. The standard deviation of the 2000–03 monthly normals for precipitation lies between 4.7% and 16.6%, which is less than the typical differences between observed and modeled precipitation.

3. Sensitivity to soil scheme

The parameterization of land surface processes in climate models is of great importance as it determines sensible and latent heat fluxes at the surface, which are the lower boundary conditions for the energy and water budgets of the atmosphere. For the GCM, the key variable of land hydrology is evaporation because it strongly controls partitioning of net incoming radiative energy into sensible and latent heat fluxes.

a. Numerical experiments

To evaluate the influence of the soil scheme, experiments with four different parameterizations are carried out. In the reference experiment (ref), the soil scheme is SECHIBA, referred to above. In the simulation denoted “b,” the SECHIBA scheme is replaced by a simple bucket model, representing the land surface as a one-layer soil reservoir, whose maximum water content W_{\max} is 150 mm. The soil moisture of the reservoir W is computed as the budget of precipitation P and evaporation E :

$$\frac{\partial W}{\partial t} = P - E, \quad (2)$$

with all the water in excess of 150 mm being lost through runoff. Evaporation is computed as

$$E = \beta \rho |\mathbf{V}| C_d [q_{\text{sat}}(T_s) - q_s], \quad (3)$$

where ρ , $|\mathbf{V}|$, C_d , q_{sat} , and q_s are, respectively, the air density, wind speed, frictional drag coefficient, and saturated relative humidity at surface air temperature, and relative humidity. Here β is an aridity function that depends on soil water content, as

$$\beta(W) = \min\left(\frac{W}{W_{\max}/2}, 1\right).$$

Two additional simulations, “b5” and “b25” are run with the same formulation for the aridity coefficient but with a soil water content fixed to 5 and 25 mm, respectively (i.e., with β fixed to 1/15 and 1/3, respectively).

b. Mean seasonal cycles

The mean seasonal cycle of temperature and relative humidity at 2 m are first compared with observations (see Fig. 3 for temperature and Fig. 4 for relative humidity). Annual cycles of air temperature and humidity simulated by the model without setting β (ref and b simulations) show more contrast than observed cycles. In particular, both parameterizations, SECHIBA and simple bucket, simulate too high temperatures associated with too low relative humidities during summer from June to September. It is noteworthy that this dry and warm bias in summer is a well-known deficiency of the LMDZ climate model over Europe (Hourdin et al. 2006). Simulation b5 also exhibits a warm and dry bias during summer. For b25, with artificially increased evaporation during the warm period, temperatures are colder and closer to observations during summer but the relative humidity is overestimated.

Note that the b5 and b25 simulations were chosen here for illustration of the sensitivity to surface evaporation. However, an intermediate value of $\beta = 10/75$

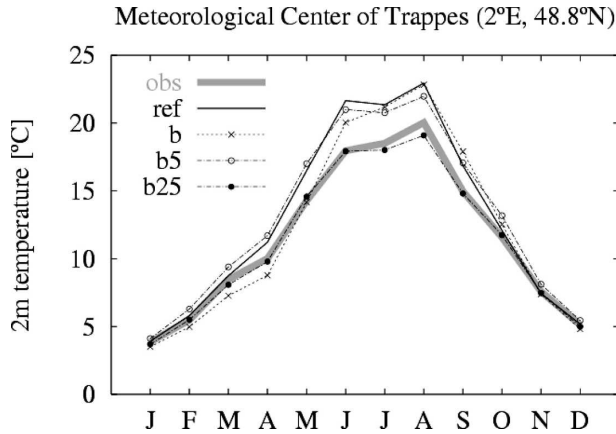


FIG. 3. Comparison between observed (obs) and simulated (ref, b, b5, and b25, see text for details) seasonal cycle of 2-m temperature.

produces better results globally, as shown in the next section.

c. Water budget

The various simulations are associated with very different evaporation rates (Fig. 5), a larger evaporation being generally associated with a colder and wetter atmosphere. Those results also strongly suggest that the SECHIBA and bucket models both underestimate surface evaporation during summer.

As suggested by De Rosnay and Polcher (1998), the low estimate of evaporation can be due to insufficient precipitation in summer, inability of the soil to store enough water during winter and/or to release water during summer, and excess of solar radiation. As shown in the last section, overestimation of solar radiation is a bias of the LMDZ model and does not depend of the soil scheme used. From consideration of the seasonal

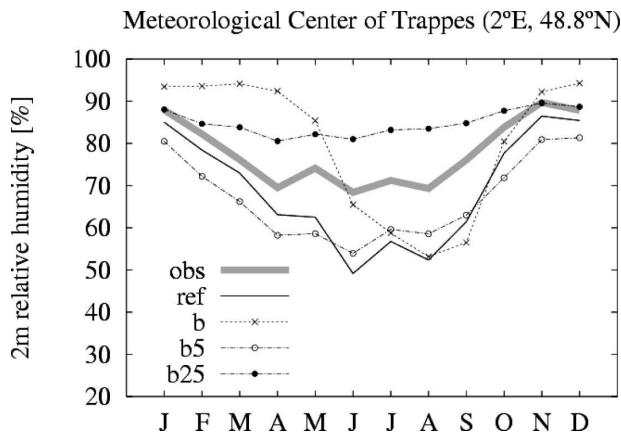


FIG. 4. Same as in Fig. 3, but for 2-m relative humidity.

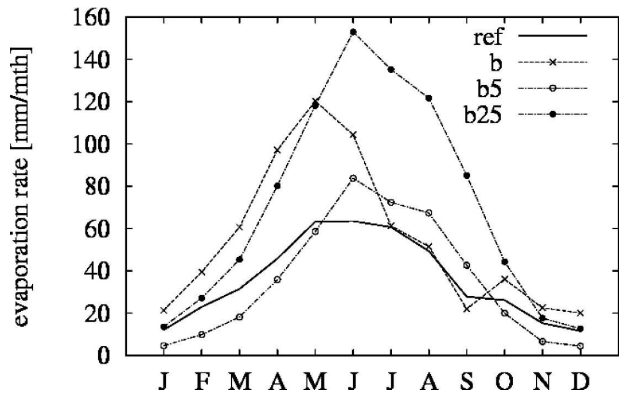


FIG. 5. Simulated seasonal cycle of evaporation rate at a position corresponding to Trappes (48.8°N, 2.0°E). As described in the text, simulations differ from each other with respect to the soil scheme employed.

cycle of soil moisture (Fig. 6) and evaporation (Fig. 5), it seems that the weak evaporation during summer with SECHIBA is explained by the soil being unable to release water from a reservoir that is always above 70% of its maximum water-holding capacity. In comparison, the low level of soil moisture in the b simulation seems to be the limiting factor for evaporation during summer.

During winter and early spring, the bucket in the b simulation is above half of its maximum content and then evaporates at the potential evaporation rate ($\beta = 1$). This high evaporation rate explains the cold and wet bias observed in spring and the subsequent rapid decrease of the soil reservoir, leading to a very low evaporation in the following summer. It is the particular dependency of the β parameter that produces the phase lag between the ref and b simulations in terms of humidity and temperature (there is no such lag for the soil water content).

The warm and dry summer bias in the ref, b, and b5

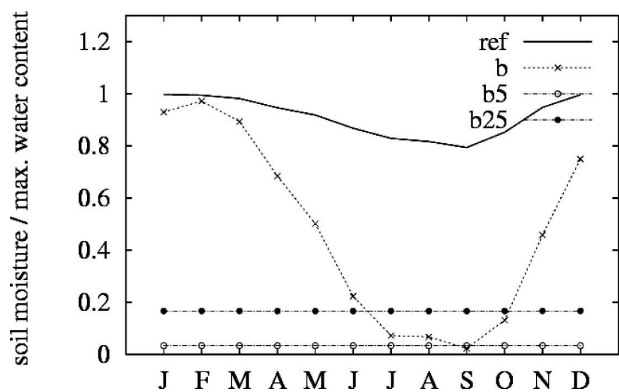


FIG. 6. Same as in Fig. 5, but for soil moisture.

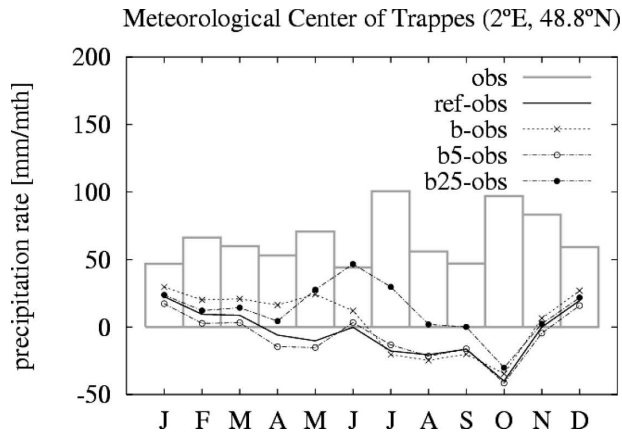


FIG. 7. Seasonal cycle of observed precipitation rates (gray bars) and differences between simulated and observed precipitation rates (see text for details on the simulations).

simulations is also associated with an underestimation of precipitation rates (Fig. 7). Increasing the evaporation rate by setting the aridity coefficient to $\frac{1}{3}$ (simulation b25) produces more precipitation, cancelling the bias in August and September but leading to an overestimation of precipitation in June–July. During early spring, the larger evaporation rates in the b simulation also produce more intense rainfalls. All simulations tend to overestimate rainfall in December and January. This overestimation is certainly partly due to a poor parameterization of large-scale precipitation processes in the model because local evaporation is expected to be less important than advection at this season. Considering vertical profiles in January (not shown here), the mean relative humidity simulated by LMDZ in the troposphere is found to be higher than ECMWF analyses. This wet bias is certainly responsible, in addition to an imperfect representation of clouds, for the precipitation overestimate in wintertime. Moreover, LMDZ inherits the defects of the ECMWF model as show in Fig. 8.

It is clear in this example that we are testing more than individual parameterizations. The larger spring evaporation in the b simulation produces a larger rainfall, which in turns increases the soil water content and surface evaporation. This loop, which is at work in the full climate GCM, can be assessed here with comparison to in situ observations.

d. Diurnal cycles

The diurnal cycle amplitude is influenced by several factors, such as cloud cover and soil moisture (Stone and Weaver 2003). By decreasing the downward solar radiation during the day and emitting longwave radiation during the night, clouds decrease the amplitude of

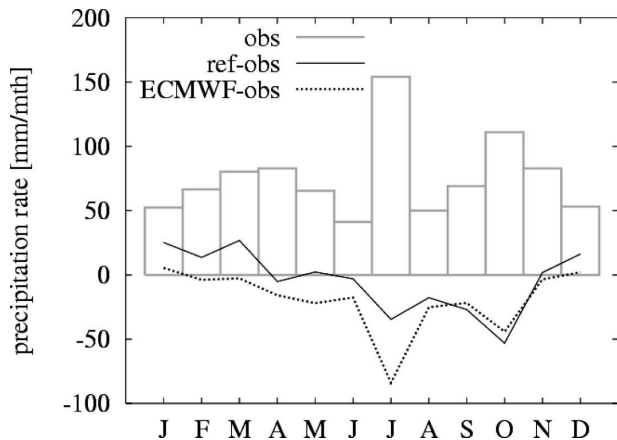


FIG. 8. Seasonal cycle (years 2000–01) of observed precipitation rates (gray bars) and differences between simulated (by the ECMWF model and the ref simulation) and observed precipitation rates.

the diurnal cycle. Soil moisture is also expected to affect the diurnal cycle by increasing both daytime surface evaporative cooling and nighttime greenhouse effect warming. The correlation between the diurnal cycle amplitude and the parameterization of the land surface scheme is examined in this section. Observed and simulated seasonal variations of the diurnal cycle amplitude are displayed in Figs. 9 (temperature) and 10 (relative humidity). The diurnal cycle amplitude is calculated as the root-mean-square deviation of the hourly values from the daily average. Comparisons of the different simulations show that the diurnal cycle amplitude is sensitive to the land surface parameterization and is strongly anticorrelated with the evaporation rate (see Fig. 5).

The amplitude of the diurnal temperature cycle is rather well simulated with the SECHIBA scheme.

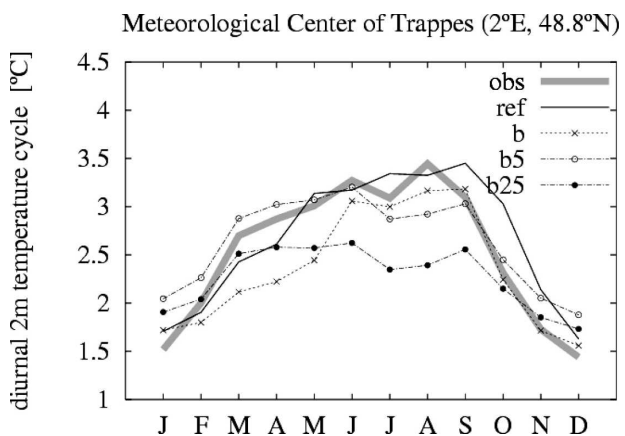


FIG. 9. Same as in Fig. 3, but for the diurnal cycle of 2-m temperature.

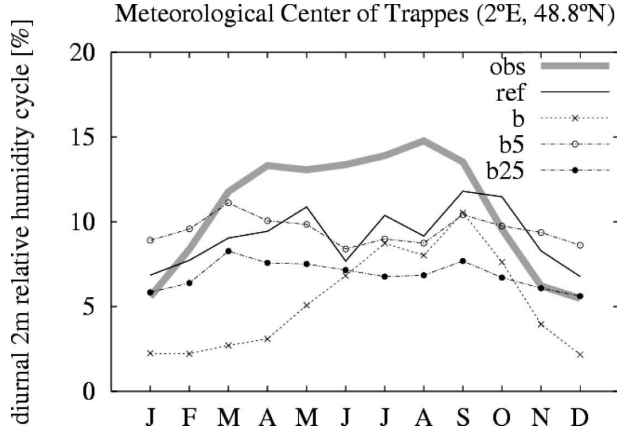


FIG. 10. Same as in Fig. 3, but for the diurnal cycle of 2-m relative humidity.

There is however a phase lag associated with an underestimation of the diurnal cycle in February–April and an overestimation in September–November. The *b* simulation is satisfactory from June to January but diurnal temperature amplitudes are too weak from February to May (months during which simulated mean temperatures are also too low). A consequence of using a constant aridity coefficient is to decrease the annual variation in diurnal temperature amplitudes. Differences between *b*, *b5*, and *b25* simulations confirm that evaporation is a controlling factor of the diurnal temperature amplitude. A larger evaporation (*b25*) reduces both the diurnal mean and the diurnal amplitude of the temperature, leading to a large underestimation of the thermal cycle amplitude in summertime.

No model succeeds in catching the seasonal cycle of the diurnal amplitude for relative humidity. The average amplitude is about right for *ref*, *b5*, and *b25* simulations but with almost no seasonal cycle whereas observations show an amplitude more than twice as large in summer than in winter. The simple bucket scheme generates a seasonal variability but not in phase with the observed one and with too small amplitudes in winter and spring.

4. Sensitivity to boundary layer scheme

In this section, we test, with the same model configuration, a new parameterization of the vertical transport in the convective PBL, based on a mass flux representation of thermal cells.

a. Parameterization of the convective boundary layer

The convective boundary layer is characterized by a flux up the gradient (upward in a mixed layer which is

either neutral or more often slightly stable). This vertical transport is dominated by strong and organized mesoscale motions (at the scale of the PBL itself). Those considerations have led in the past to a number of adaptations or alternatives to the diffusive approach. Deardorff (1972) proposed introducing a countergradient term to obtain upward heat fluxes even in a slightly stable atmosphere. This countergradient approach has been refined further by Troen and Mahrt (1986) and Holtslag and Boville (1993). Stull (1984) proposed to cut radically with the diffusive approach by allowing direct exchanges between all the layers in the PBL. The transient matrix framework he proposed has led to several interesting attempts in terms of parameterizations (Pleim and Chang 1992; Alapaty et al. 1997).

Mass flux ideas, originally developed for cumulus convection, have led to various parameterizations of the PBL. The concept of mass flux approaches consists of explicitly describing subgrid-scale vertical mass fluxes used afterward to transport atmospheric quantities such as potential temperature, water, momentum, or atmospheric constituents. For the convective PBL, the column is generally divided into an ascending buoyant plume, with mass flux $f = \alpha \rho w$, where α , ρ , and w are the fractional cover, air density, and vertical velocity in the thermal plume, respectively, and a compensating subsidence in the environment of mass flux $-f$. With these notations, the subgrid-scale turbulent flux of a quantity φ reads as

$$\overline{\rho w' \varphi'} = f(\hat{\varphi} - \check{\varphi}), \quad (4)$$

$$= \frac{1}{1 - \alpha} f(\hat{\varphi} - \varphi), \quad (5)$$

where $\hat{\varphi}$ is the value of φ inside the buoyant plume and $\check{\varphi}$ in its environment with $\varphi = \alpha \hat{\varphi} + (1 - \alpha)\check{\varphi}$. These equations can be considered as a general framework for the mass flux application to the PBL.

This framework has been applied in the past essentially in the form of bulk models in which it is assumed that, in the mixed layer, the various quantities are constant (Betts 1973; Lilly 1968; Randall et al. 1992) or vary linearly (Albrecht 1979; Wang and Albrecht 1990) as a function of height. In those approaches, the mass flux parameterization was used to prescribe an entrainment flux at the top of the PBL. Bulk mass flux models were generally derived to analyze the physics of the PBL but some were also used as real parameterizations for circulation models (Suarez et al. 1983).

The mass flux approach retained by Hourdin et al. (2002) differs from those previous studies by many aspects. First, the thermal plume model does not intend to account for all the turbulent motions in the PBL. A

diffusive formulation is kept in the model, which accounts in particular for small-scale turbulent transfers in the surface layer. Second, the mass flux is computed explicitly from the buoyancy of warmer air taken in the surface layer and transported through atmospheric layers, to the level of neutral buoyancy. Overshoot is also explicitly computed above that level. In that respect, the model is closer to some of the mass flux approaches retained for the representation of cumulus convection (Arakawa and Schubert 1974; Emanuel 1991; Tiedtke 1989).

A similar two-stream framework in which a mass flux computation coexists with a turbulent diffusion was already proposed by Chatfield and Brost (1987). In this work, the mass flux profiles were prescribed as a function of z/z_i (where z_i is the inversion height) based on similarity ideas. This parameterization was apparently not tested in circulation models. A parameterization still closer to the thermal plume model of Hourdin et al. (2002) has since been developed independently by A. P. Siebesma and J. Teixeira (2005, personal communication) and tested by Soares et al. (2004).

Last, note that the idea of mass fluxes was applied by Randall et al. (1992) and Lappen and Randall (2001) who tried to combine the kinetic energy equation with a mass flux approach in order to derive closure relationships for the mass flux and width of the thermals. The mass flux approach was also used by Abdella and McFarlane (1997) to derive a third-order closure of the turbulent equations.

b. Numerical experiments

To evaluate the influence of the boundary layer scheme, we ran experiments with two versions of the PBL scheme. Both parameterizations were tested with the SECHIBA surface scheme and the bucket model with a constant aridity coefficient $\beta = 10/75$. For both cases, the vertical boundary layer flux of a quantity φ can be written formally as

$$\overline{\rho w' \varphi'} = -\rho K_\varphi \left(\frac{\partial \varphi}{\partial z} - \Gamma_\varphi \right) + f(\hat{\varphi} - \varphi). \quad (6)$$

Note that we use the classical approximation $\alpha \ll 1$ for the mass flux parameterization.

In ref (same as in the previous section) and b10 simulations, the standard parameterization is used: the coefficient K_φ depends on wind shear and the Richardson number according to Laval et al. (1981), a constant countergradient term $\Gamma_\theta = 1 \text{ K km}^{-1}$ is applied for potential temperature and the mass flux f is set to 0.

In the “ref + th” and “b10 + th” simulations, K_φ is defined by parameterization 2.5 in Mellor and Yamada

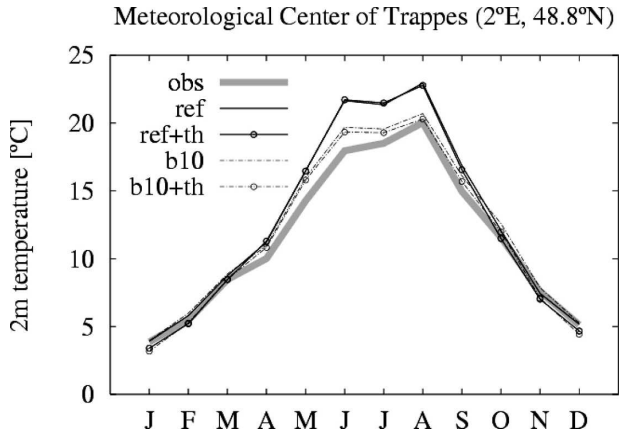


FIG. 11. Comparison between observed (obs) and simulated (ref, ref + th, b10, and b10 + th, see text for details) seasonal cycle of 2-m temperature.

(1974) based on a prognostic equation for the turbulent kinetic energy, the thermal plume model ($f \neq 0$) and no countergradient ($\Gamma = 0$). The mass flux f is computed with a modified version of the thermal plume model of Hourdin et al. (2002) as described in the appendix. When compared with academic LES of the convective PBL (Hourdin et al. 2002), a significant improvement is already observed when using the Mellor–Yamada scheme alone (i.e., without the thermal plume model) instead of the standard LMDZ parameterization. Vertical profiles of potential temperature and heat flux are in good agreement with results of LES published by Ayotte et al. (1996). In contrast, the standard parameterization leads to unstable atmospheres when surface heating is too significant (the constant counter gradient term being unefficient). The Mellor–Yamada scheme alone nevertheless underestimates entrainment and leads to a too sharp inversion. Combining this diffusive scheme with the thermal plume model improves the vertical structure of the mixed-layer and top entrainment. An examination of the simulated thermals structure indicates that heat is first supplied from the surface to the surface layer by the diffusion scheme and then transported in the mixed layer by thermals.

c. Mean seasonal cycles

The use of a different parameterization of the boundary layer scheme does not produce significant differences in mean temperatures (Fig. 11) and humidities (Fig. 12). The sensitivity to the PBL scheme is larger in winter where the new parameterization produces a slightly wetter and colder climate. In wintertime, the thermal plume model is generally not active. Differences between the standard and the new parameteriza-

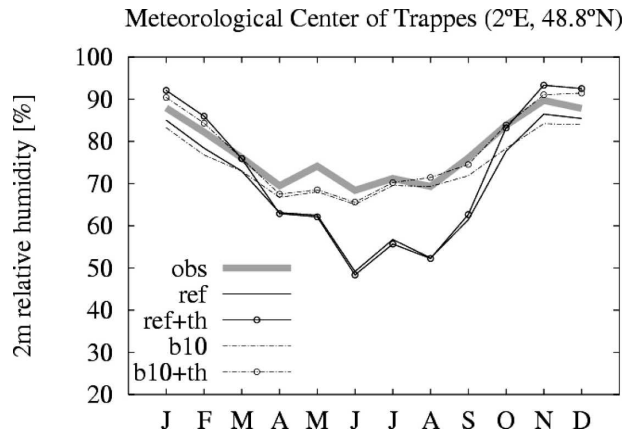


FIG. 12. Same as in Fig. 11, but for 2-m relative humidity.

tion are consequently mainly due to the change in the diffusion scheme. An examination of vertical profiles in winter indicates that local mixing in the surface layer is more important with the Mellor–Yamada scheme and extends up lower in the troposphere. In summertime, mean temperature and relative humidity are less sensitive to the boundary layer parameterization than to the representation of land surface processes. The best agreement with observations is thus obtained with the bucket model with a constant aridity coefficient $\beta = 10/75$. The b10 + th simulation is somewhat better than b10. The only difference in the water budget between the two different boundary layer parameterizations (not shown here) is a slight increase in evaporation during summer with the thermal plume model. This leads to an increased rainfall amount and higher soil moisture.

d. Diurnal cycles

Figure 13 shows the differences of the mean seasonal cycle of the thermal diurnal cycle between model runs and observations. The annual cycle is strongly influenced by the PBL parameterization. Use of the mass flux representation of thermal, associated with the Mellor–Yamada scheme for the turbulence exchange leads to lower diurnal cycles from October to February and to higher cycles from March to September. The SECHIBA land surface scheme results in overestimated diurnal cycles in spring and summer. The simple bucket model leads to a good agreement with observations, in spite of an underestimation in July–August. Figure 14 displays the mean seasonal cycle of the diurnal cycle of relative humidity. The new parameterization enhances the annual cycle with amplitude of the diurnal cycle higher in spring and summer. Compared with the b10 simulation, results of b10 + th are significantly improved with a more realistic annual cycle, but

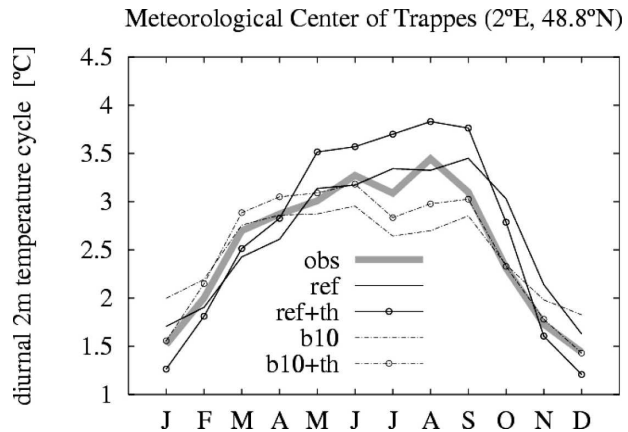


FIG. 13. Same as in Fig. 11, but for seasonal variation of the diurnal cycle of 2-m temperature.

the diurnal cycle is still underestimated in summer. The study of hourly simulated temperature and relative humidity during the VAPIC observation period shows that the improvement is due to both the Mellor–Yamada scheme and the thermal plume model. On the one hand, using the Mellor–Yamada parameterization as the diffusion scheme produces a wetter nocturnal surface layer. On the other hand, the thermal flux model, by transporting humidity from the surface to the mixed layer leads to a drier surface layer during daytime. Combining the Mellor–Yamada scheme and the thermal flux model produces a surface layer that is wetter during nighttime, drier during daytime, and in agreement with observations. The resulting 2-m relative humidity cycle is consequently well caught. The b10 + th parameterization is the most appropriate to simulate the mean meteorological parameters (temperature and relative humidity) and the diurnal cycle amplitude. The warm bias of the reference experiment is significantly reduced, even if the model remains too

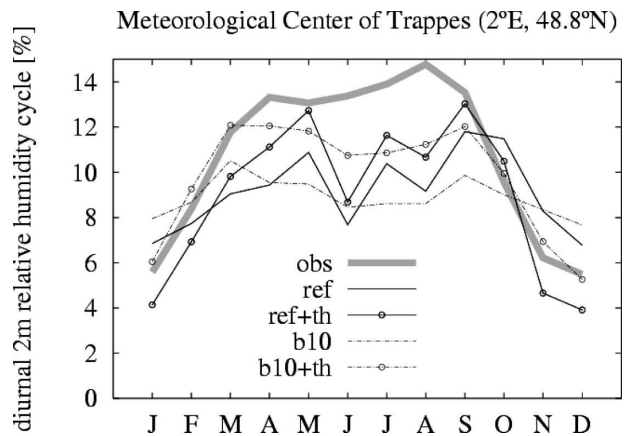


FIG. 14. Same as in Fig. 13, but for 2-m relative humidity.

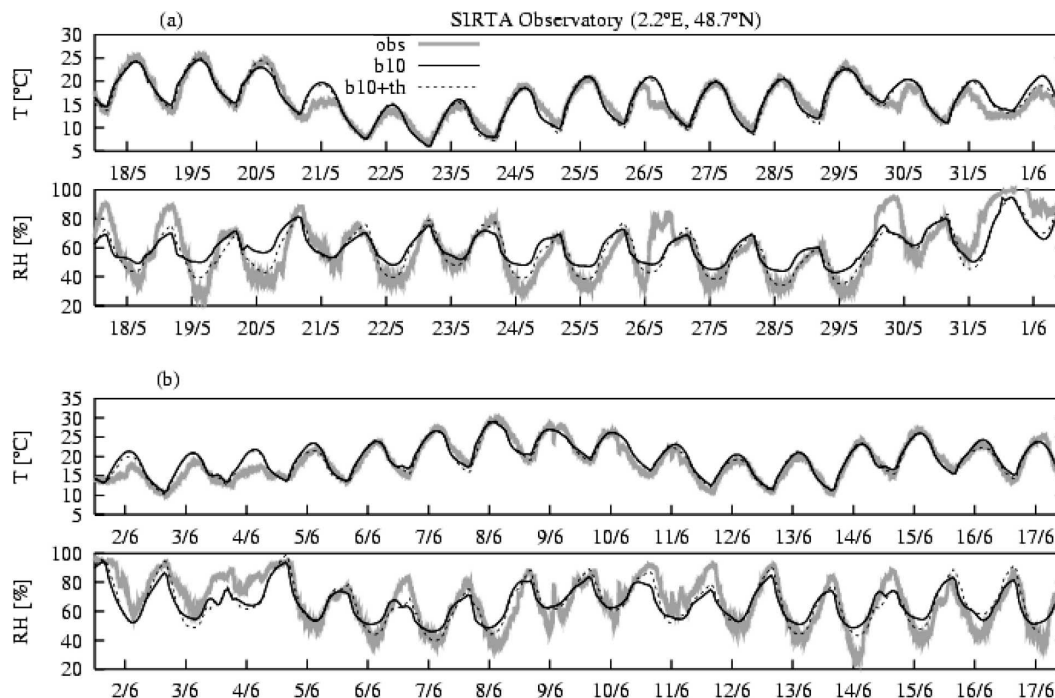


FIG. 15. Observed and 2-m simulated temperature (T) and relative humidity (RH) for (a) 18 May 2004–1 Jun 2004 and (b) 2–17 Jun 2004. Measurements are performed 15 m above ground.

warm from April to July. The annual cycle of the diurnal amplitude of temperature is in phase with the observed one and the simulated values are close to measurements.

5. Comparison with SIRTA observations

To illustrate the performances of the model with the optimum parameterization (b10 + th), a 1-month period, corresponding to the VAPIC intensive observation period, has been more precisely studied. During this period, running from 18 May 2004 to 17 June 2004, observations performed by remote sensing and in situ instruments at the SIRTA observatory (weather station, cloud aerosol lidar, radiosonde measurements, and flux meters) are used to analyze simulated surface temperature, humidity, PBL height, and shortwave fluxes. We focus in this section on the b10 and b10 + th simulations. The physical parameterization is the same as previously. However, we decreased the time step for computation of meteorology (i.e., 1 min instead of 1.5) and physical processes (3 min instead of 30) to avoid numerical instabilities in the computation of PBL heights.

a. Temperature and humidity

As shown in Fig. 15, simulated temperatures and relative humidities are in satisfactory agreement with

observations. Amplitude of the diurnal cycle of humidity is enhanced with the thermal plume model, whereas there are no significant differences in the two simulated temperatures. Daytime temperatures are sometimes overestimated (21 and 26 May and from 30 May to 4 June) and these periods are also associated with underestimated relative humidities. Daytime humidities are nevertheless well captured when using the thermal plume model. Nighttime minimum temperatures are close to observed data, whereas maximum humidities are generally underestimated by the model. In spite of the slight underestimation of the amplitude of the diurnal cycle of humidity, the phase characteristics of the diurnal cycle are well captured by the model.

b. Boundary layer height

1) BOUNDARY LAYER HEIGHT DETECTION

Two methods are used to retrieve the PBL height. The first one is based on a dual-wavelength (532 and 1064 nm) backscattering lidar and the other one makes use of radiosonde profiles.

Aerosols in the atmosphere are efficient scatterers of lidar pulses. The sharp decrease of aerosol concentration often observed at the interface between the PBL and the free troposphere results in a marked decrease of the lidar backscattered signal at the top of the PBL. At night however, the PBL can be quite shallow while

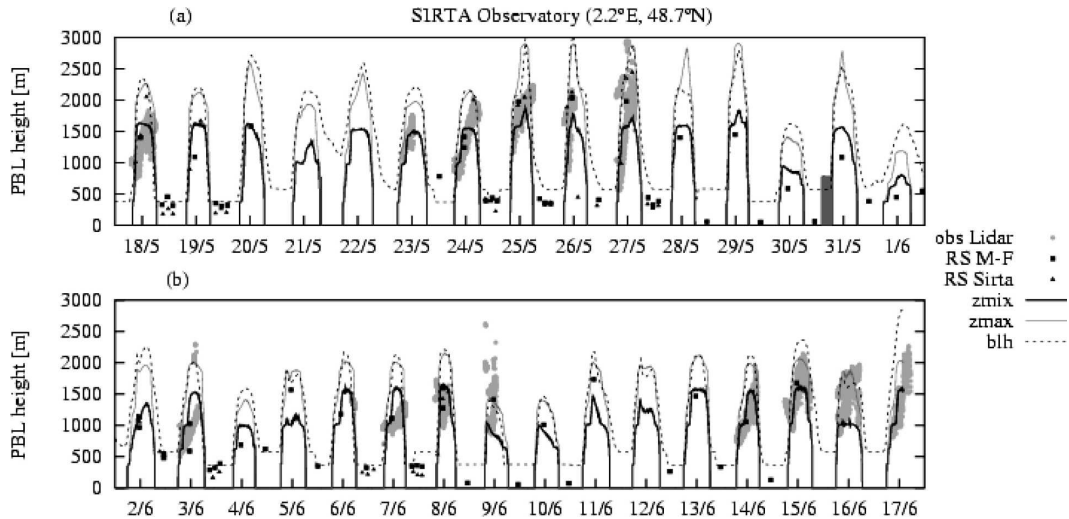


FIG. 16. Comparison between observed and simulated PBL height (a) from 18 May to 1 Jun 2004 and (b) from 2 to 17 Jun 2004. Observations are derived from the backscattering lidar (gray points), radiosondes measurements from the meteorological center of Météo-France (square dots), and from the SIRTa observatory (triangle dots), z_{mix} (black line) is the height of null buoyancy, z_{max} (gray line) the top of the plume (see the appendix for details), and blh (dashed line) the boundary layer height calculated as described by Mathieu et al. (2004).

aerosols remain aloft in stratified layer called residual layer. In this case, the sharp transition in the lidar backscattered signal occurs at the top of the residual layer. In other situations clouds can reside at or near the top of the PBL, which causes the lidar signal to increase rather than decrease in the transition region. Morille et al. (2007) developed a multiple-test algorithm to identify cloud and aerosol layers, to detect vertical zones that are nearly particle free, and to estimate the altitude of the PBL top. This algorithm makes use of wavelet transform to identify singularities in the lidar backscattered profiles and searches coherence in the multiple tests to identify the different particle layers. While the Morille et al. (2007) algorithm is efficient at estimating the PBL height in the presence of clouds, it is not able to distinguish between the top of the boundary layer and the residual layer.

The method used to extract PBL height from radiosonde measurements is a threshold method applied on a bulk Richardson number $Ri_b(z)$ calculated as

$$Ri_b(z) = \frac{g(z - z_0) [\theta(z) - \theta(z_0)]}{\theta(z) [u(z)^2 + v(z)^2]}, \quad (7)$$

where θ is the potential temperature, g is the acceleration due to gravity, z is the height, z_0 is the altitude reference (considered here as the first vertical point available on the sounding profile), and u and v are the zonal and meridional wind components, respectively. The PBL height is estimated with a threshold value of 0.21 (Vogelezang and Holtslag 1996).

2) RESULTS AND DISCUSSION

The boundary layer height, extracted from radiosonde measurements and lidar retrievals, is compared with output of the model run in Fig. 16. The PBL height is at its minimum throughout the night, increases to its daytime maximum because of diurnal heating, and then decreases at sunset. For most of the days, the observed daytime PBL is comprised between the altitude of neutral buoyancy z_{mix} and top of thermal plume z_{max} (see the appendix for the definition of z_{mix} and z_{max}). The model succeeds in simulating the daily variability of the PBL pulse in response to different meteorological conditions. For instance, during the 25–27 May period, the PBL extends up to 2000–2500 m and the model forecasts the maximum PBL height to be about 2800 m. In contrast, the PBL height reaches only 1300 m on 3 June, 600 m lower than the maximum predicted by the model (1900 m). The height of the mixed layer forecast by the model is nevertheless slightly overestimated on this day: simulated temperatures are also too high, which can explain a too efficient mixing. The reverse situation occurs on 9–10 June with a PBL height predicted by the model lower than the observed one. During this period, simulated temperatures are however in good agreement with observations. In general, the growth rate for the mixing layer is well predicted by the model (especially during the 23–27 May and the 14–17 June periods). At night, the simulated PBL (“ blh ” in Fig. 16) is in good agreement with observations extracted from radiosonde measurements. Note that z_{mix} and z_{max}

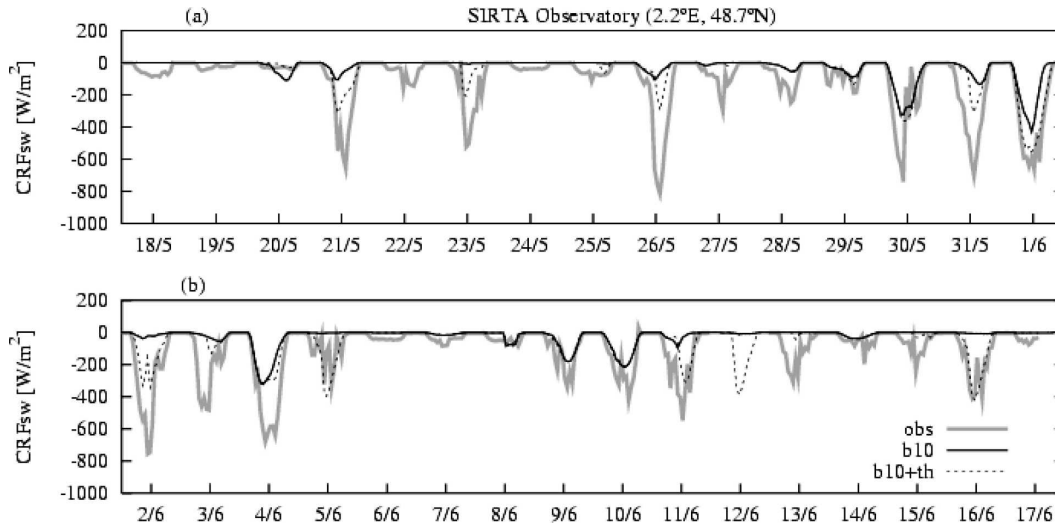


FIG. 17. Observed and simulated shortwave cloud radiative forcing (CRFsw) (a) from 18 May to 1 Jun 2004 and (b) from 2 to 17 Jun 2004.

are null throughout the night because thermals are not active during this period. The simulation sometime overestimates the height of the very stable nocturnal boundary layer.

The “th” boundary layer scheme associated with the simple bucket scheme with a constant soil moisture set to 10 mm is thus able to simulate the height of the PBL quite well during the intensive observation period. Some episodes are nevertheless not captured by the model (e.g., overestimation on 9–10 June).

c. Shortwave cloud forcing

Figure 17 displays the shortwave cloud radiative forcing. The forcing is calculated with respect to the clear-sky shortwave radiation computed by the model. Daily variability is well captured by the model, in spite of a systematic underestimation of the simulated cloud radiative forcing. This is particularly true on days during which temperatures are overestimated (21, 26, 31 May and 4 June). A poor estimation of the cloud fraction on these days could explain the overestimation of the shortwave fluxes and, consequently, of the temperatures. Nevertheless, the cloud cover is improved when using the thermal plume model. This new parameterization significantly improves top entrainment (Hourdin et al. 2002) and vertical profiles of relative humidity. After having computed vertical transport with the thermal plume model, occurrence of oversaturation is checked. In this case, condensation takes place and the LMDZ cloud scheme is used to diagnose the occurrence of clouds. With this representation of dry convection, more low and middle clouds are simulated, leading to an increased cloud forcing. On 23 May and 5 and 16

June, no cloud cover is predicted by the b10 simulation, whereas the thermal plume model diagnoses a nonzero cloud forcing, close to the observations. But some cloudy episodes remain uncaptured with this parameterization (e.g. 26 May).

6. Conclusions

In this study, we performed simulations using a variable resolution GCM, LMDZ, with different parameterizations of land surface and boundary layer processes. The model was run with its zooming capability to reach 120-km resolution in the region of interest (the vicinity of Paris). One objective of this work was to adjust the parameterization schemes to produce the best possible simulation (with no updates of initial conditions during the simulation period). Different land surface schemes were first tested. The best agreement with observations is obtained with the bucket model with a constant aridity coefficient $\beta = 10/75$. The computation of soil moisture as the budget of rainfall and evaporation (simulations “ref” and “b”) seems to have a seasonal inertia that is too weak leading to overly contrasted 2-m temperature and humidity annual cycles. A second part was devoted to the sensitivity analysis of the boundary layer parameterization. The simulated diurnal cycles are enhanced by using the thermal plume model associated with the Mellor–Yamada scheme for small-scale turbulence, providing better agreement with observations. This parameterization of the boundary layer leads to realistic seasonal cycles of the mean temperature and humidity as well as of their diurnal variations. The evaluation was first per-

formed on a 4-yr period (from 1 January 2000 to 31 December 2003) and then on 1-month period (from 18 May 2004 to 17 June 2004), corresponding to an intensive observation period. During this period, we compared hourly observations of the SIRTAs observatory with predicted temperatures, relative humidities, boundary layer heights, and shortwave fluxes. The “b10 + th” succeeds in catching most day-to-day variations.

This simulation will be used further as a basis for improving the cloud scheme of the LMDZ model and of its coupling with the new thermal plume model. In this new representation of thermals (under development), the latent heat release inside the plume when water condenses is accounted for. The version used in this study, developed for dry convection (Hourdin et al. 2002), already improves the representation of boundary layer clouds, but still underestimates the total cloud cover, which could significantly contribute to the warm bias observed in summer over the Paris area. The measurement of turbulent fluxes available since spring 2005 at SIRTAs will be of great help to further constrain the surface scheme.

Besides the particular results obtained with LMDZ, the study presented here underlines the potentiality of using a climate model with a nudging and zooming capability to work on physical parameterizations. This framework allows a fully coupled set of parameterizations to be assessed on a given synoptic situation with a very low human and numerical cost. It is noteworthy that both the warm bias and the underestimation of the shortwave cloud radiative forcing are also observed when the same model (LMDZ) is used in a climate mode. Comparing day-by-day observations with model outputs allows us to identify which of the parameterizations is responsible for these biases and to easily assess new developments.

Acknowledgments. The author acknowledges A. Dabas and J.-P. Aubagnac from the Centre National de Recherche en Météorologie for providing the radiosondes launched from SIRTAs during the VAPIC campaign and the high-resolution radiosonde data. We acknowledge Météo-France for providing radiosonde data from the departmental station of Trappes. Thanks are extended to the SIRTAs team for providing processed geophysical parameters for our study.

APPENDIX

The Thermal Plume Model

The thermal plume model described by Hourdin et al. (2002) has been modified in order to simplify calculations, to reduce central processing unit (CPU) time,

and to improve robustness. The physical processes involved stay unchanged, only the computation of the thermal plume characteristics is different.

A thermal plume is made of buoyant air coming from the unstable surface layer. The first step consists in determining the vertical mass flux $f = \alpha\rho w$ in the thermal between each layer. The continuity equation for the thermal plume is written as

$$\frac{\partial f}{\partial z} = e - d, \quad (\text{A1})$$

where e represents the entrainment rate at which air is supplied to the base of the thermal plume and d is the detrainment rate from the thermal into the environment. The computation of the thermal properties is first done for $d = 0$. It is this first step that is modified in the new version.

In the original version of the thermal plume model described by Hourdin et al. (2002) a buoyant plume is computed starting from each unstable layer near the surface (a layer the potential temperature of which is higher than that of the layer just above). Those independent plumes are then combined to produce a mean thermal that is used afterward to compute the vertical transport of potential temperature, momentum, water, and tracers.

In the new version we directly compute the properties of the mean thermal by imposing a priori the vertical distribution of the entrainment rate at the basis of the plume specified as $e = \phi e^*$ with $\int_0^\infty e^* dz = 1$. The knowledge of the normalized entrainment e^* is sufficient to determine the air properties and vertical velocity inside the thermal plume. Parameter ϕ , which is also the mass flux above the entrainment layer, is determined afterward from a closure relationship.

The different steps of the calculation are the following.

- 1) Definition of the discrete entrainment rate integrated over the width Δz_k of layer k , $E_k^* \approx e_k^* \Delta z_k$, in each unstable layer of the model (for which $\Delta^+ \theta_k = \theta_{k+1} - \theta_k < 0$). In the present simulations $E_k^* = \Xi \max(\Delta^+ \theta_k, 0) \Delta z_k$, where Ξ is chosen in order to have $\sum E_k^* = 1$.
- 2) Determination of the virtual potential temperature $\hat{\theta}$ and vertical velocity w inside the plume at each level (θ is the virtual potential temperature in the environment). Potential temperature is computed from the conservation equation:

$$\hat{\theta}_l = \frac{\sum_{k=1}^{k=l} E_k^* \theta_k}{F_{l+1/2}^{c*}}, \quad (\text{A2})$$

where

$$F_{l+1/2}^{c*} = \sum_{k=1}^{k=l} E_k^* \quad (\text{A3})$$

is the conservative (computed with no detrainment) mass flux in the thermal. For the vertical velocity and for a stationary plume, the vertical variation of the kinetic energy must be equal to the work of buoyant forces:

$$\frac{1}{2} w_{l+1/2}^2 = \frac{1}{2} \left(\frac{F_{l-1/2}^{c*}}{F_{l+1/2}^{c*}} w_{l-1/2} \right)^2 + g \frac{\hat{\theta}_l - \theta_l}{\theta_l} (z_{l+1/2} - z_{l-1/2}). \quad (\text{A4})$$

The factor $F_{l-1/2}^{c*}/F_{l+1/2}^{c*}$ accounts for the fact that the air entrained in layer l enters the thermal plume with a zero vertical velocity. It is then possible to compute the height z_{mix} of null buoyancy where the velocity is maximal (w_{max}) and the top of the plume z_{max} , defined as the height where the vertical velocity cancels. To reduce numerical instability z_{max} and z_{mix} are defined as continuous and not discrete values as was the case in the old version.

- 3) The closure consists in determining the coefficient ϕ . From considerations of the geometry of thermal rolls in a 2D configuration, the entrainment rate is related to the velocity v_k of lateral entrainment and the width of one thermal cell $L = rz_{\text{max}}$ (r being the aspect ratio of the cell) as

$$E_k = \phi E_k^* = \frac{\rho_k \Delta z_k v_k}{rz_{\text{max}}}. \quad (\text{A5})$$

The closure relationship is based on the identity of the maximum vertical velocity in the thermal plume and mean horizontal velocity in the entrainment layer:

$$w_{\text{max}} = \sum E_k^* v_k. \quad (\text{A6})$$

Combining those two relationships finally leads to

$$\phi = \frac{w_{\text{max}}}{rz_{\text{max}} \sum \frac{E_k^{*2}}{\rho_k \Delta z_k}}. \quad (\text{A7})$$

- 4) The true entrainment rate $E_k = \phi E_k^*$ and conservative mass flux $F_k^c = \phi F_k^{c*}$ can then be computed. The detrainment and vertical transport are finally computed as in Hourdin et al. (2002).

REFERENCES

- Abdella, K., and N. McFarlane, 1997: A new second-order turbulence closure scheme for the planetary boundary layers. *J. Atmos. Sci.*, **54**, 1850–1867.
- Ackerman, T., and G. Stokes, 2003: The atmospheric radiation measurement program. *Phys. Today*, **56**, 38–45.
- Alapaty, K. A., J. E. Pleim, S. Raman, D. S. Niyogi, and D. W. Byun, 1997: Simulation of atmospheric boundary layer processes using local and nonlocal-closure schemes. *J. Appl. Meteor.*, **36**, 214–233.
- Albrecht, B. A., 1979: A model of the thermodynamic structure of the trade-wind boundary layer: Part II: Applications. *J. Atmos. Sci.*, **36**, 90–98.
- Arakawa, R. A., and W. H. Schubert, 1974: Interaction of a cumulus cloud ensemble with the large scale environment, Part I. *J. Atmos. Sci.*, **31**, 674–701.
- Ayotte, K. W., and Coauthors, 1996: An evaluation of neutral and convective planetary boundary-layer parameterizations relative to large eddy simulations. *Bound.-Layer Meteor.*, **79**, 131–175.
- Betts, A. K., 1973: Non-precipitating convection and its parameterization. *Quart. J. Roy. Meteor. Soc.*, **99**, 178–196.
- Bony, S., and K. A. Emanuel, 2001: A parameterization of the cloudiness associated with cumulus convection; evaluation using TOGA COARE data. *J. Atmos. Sci.*, **58**, 3158–3183.
- Chatfield, R. B., and R. A. Brost, 1987: A two-stream model of the vertical transport of trace species in the convective boundary layer. *J. Geophys. Res.*, **92**, 13 263–13 276.
- Chiriac, M., R. Vautard, H. Chepfer, M. Haefelin, J. Dudhia, Y. Wanherdrick, Y. Morille, and A. Protat, 2006: The ability of MM5 to simulate ice clouds: Systematic comparison between simulated and measured fluxes and lidar/radar profiles at the SIRTAt atmospheric observatory. *Mon. Wea. Rev.*, **134**, 897–918.
- Deardorff, J. W., 1972: Theoretical expression for the countergradient vertical heat flux. *J. Geophys. Res.*, **77**, 5900–5904.
- De Rosnay, P., and J. Polcher, 1998: Modelling root water uptake in a complex land surface scheme coupled to a GCM. *Hydrol. Earth Syst. Sci.*, **2**, 239–255.
- Ducharne, A., and K. Laval, 2000: Influence of the realistic description of soil water-holding capacity on the global water cycle in a GCM. *J. Climate*, **13**, 4393–4413.
- Ducoudré, N., K. Laval, and A. Perrier, 1993: SECHIBA, a new set of parameterizations of the hydrologic exchanges at the land-atmosphere interface within the LMD atmospheric general circulation model. *Climate Dyn.*, **6**, 248–273.
- Emanuel, K. A., 1991: A scheme for representing cumulus convection in large-scale models. *J. Atmos. Sci.*, **48**, 2313–2335.
- Fouquart, Y., and B. Bonnel, 1980: Computations of solar heating of the earth's atmosphere: A new parametrization. *Contrib. Atmos. Phys.*, **53**, 35–62.
- Gates, W. L., 1992: AMIP: The Atmospheric Model Intercomparison Project. *Bull. Amer. Meteor. Soc.*, **73**, 1962–1970.
- Ghan, S. J., L. R. Leung, and J. McCaa, 1999: A comparison of three different modeling strategies for evaluating cloud and radiation parameterizations. *Mon. Wea. Rev.*, **127**, 1967–1984.
- Guichard, F., D. Parsons, J. Duhdia, and J. Bresch, 2003: Evaluating mesoscale model predictions of clouds and radiation with SGP ARM data over a seasonal timescale. *Mon. Wea. Rev.*, **131**, 926–944.
- , and Coauthors, 2004: Modelling the diurnal cycle of deep precipitating convection over land with cloud-resolving mod-

- els and single-column models. *Quart. J. Roy. Meteor. Soc.*, **130**, 3139–3172.
- Haefelin, M., and Coauthors, 2005: SIRTA, a ground-based atmospheric observatory for cloud and aerosol research. *Ann. Geophys.*, **23**, 253–275.
- Hoke, J. E., and R. A. Anthes, 1976: The initialization of numerical models by a dynamic-initialization technique. *Mon. Wea. Rev.*, **104**, 1551–1556.
- Holtzlag, A. A. M., and R. A. Boville, 1993: Local versus nonlocal boundary layer diffusion in a global climate model. *J. Climate*, **6**, 1825–1842.
- Hourdin, F., P. Le Van, F. Forget, and O. Talagrand, 1993: Meteorological variability and the annual surface pressure cycle on Mars. *J. Atmos. Sci.*, **50**, 3625–3640.
- , F. Couvreux, and L. Menut, 2002: Parameterization of the dry convective boundary layer based on a mass flux representation of thermals. *J. Atmos. Sci.*, **59**, 1105–1123.
- , and Coauthors, 2006: The LMDZ4 general circulation model: Climate performance and sensitivity to parametrized physics with emphasis on tropical convection. *Climate Dyn.*, **27**, 787–813.
- Jeuken, A. B. M., P. C. Siegmund, L. C. Heijboer, J. Feichter, and L. Bengtsson, 1996: On the potential of assimilating meteorological analyses in a global climate model for the purpose of model validation. *J. Geophys. Res.*, **101**, 16 939–16 950.
- Kasahara, A., 1977: Computational aspects of numerical models for weather prediction and climate simulation. *Methods Comput. Phys.*, **17**, 1–66.
- Krinner, G., and Coauthors, 2005: A dynamic global vegetation model for studies of the coupled atmosphere–biosphere system. *Global Biogeochem. Cycles*, **19**, GB1015, doi: 10.1029/2003GB002199.
- Lappen, C., and D. A. Randall, 2001: Toward a unified parameterization of the boundary layer and moist convection. Part I: A new type of mass-flux model. *J. Atmos. Sci.*, **58**, 2021–2036.
- Laval, K., R. Sadourny, and Y. Serafini, 1981: Land surface processes in a simplified general circulation model. *Geophys. Astrophys. Fluid Dyn.*, **17**, 129–150.
- Lenderink, G., and Coauthors, 2004: The diurnal cycle of shallow cumulus clouds over land: A single-column model intercomparison study. *Quart. J. Roy. Meteor. Soc.*, **130**, 3339–3364.
- Lilly, D. K., 1968: Models of cloud-topped mixed layers under a strong inversion. *Quart. J. Roy. Meteor. Soc.*, **94**, 292–309.
- Manabe, S., 1969: Climate and the ocean circulation. 1. The atmospheric circulation and the hydrology of the Earth's surface. *Mon. Wea. Rev.*, **97**, 739–774.
- Marti, O., and Coauthors, 2005: The new IPSL climate system model: IPSL-CM4. Tech. Note 26, IPSL, 82 pp. [Available online at <http://dods.ipsl.jussieu.fr/omamce/IPSLCM4/DocIPSLCM4/>]
- Mathieu, A., A. Lahellec, and A. Weill, 2004: Evaluation of a numerical weather forecast model using boundary layer cloud top temperature retrieved from AVHRR. *Mon. Wea. Rev.*, **132**, 915–928.
- Mellor, G. L., and T. Yamada, 1974: A hierarchy of turbulence closure models for planetary boundary layer. *J. Atmos. Sci.*, **31**, 1791–1806.
- Morcrette, J. J., 2002: Assessment of the ECMWF model cloudiness and surface radiation fields at the ARM SGP site. *Mon. Wea. Rev.*, **130**, 257–277.
- , L. Smith, and Y. Fouquart, 1986: Pressure and temperature dependence of the absorption in longwave radiation parameterizations. *Contrib. Atmos. Phys.*, **59**, 455–469.
- Morille, Y., M. Haefelin, P. Drobinski, and J. Pelon, 2007: STRAT: An automated algorithm to retrieve the vertical structure of the atmosphere from single-channel lidar data. *J. Atmos. Oceanic Technol.*, in press.
- Ohmura, A., and Coauthors, 1998: Baseline surface radiation network (BSRN/WCRP): New precision radiometry for climate research. *Bull. Amer. Meteor. Soc.*, **79**, 2115–2136.
- Pleim, J. E., and J. S. Chang, 1992: A non-local closure model for vertical mixing in the convective boundary layer. *Atmos. Environ.*, **26A**, 965–981.
- Randall, D. A., Q. Shao, and C. Moeng, 1992: A second-order bulk boundary layer model. *J. Atmos. Sci.*, **49**, 1903–1923.
- Sadourny, R., and K. Laval, 1984: January and July performance of the LMD general circulation model. *New Perspectives in Climate Modelling*, A. Berger and C. Nicolis, Eds., Elsevier, 173–198.
- Simmons, A. J., and D. M. Burridge, 1981: An energy and angular-momentum conserving vertical finite-difference scheme and hybrid vertical coordinates. *Mon. Wea. Rev.*, **109**, 758–766.
- Soares, P. M. M., P. M. A. Miranda, A. P. Siebesma, and J. Teixeira, 2004: An eddy-diffusivity/mass-flux parametrization for dry and shallow cumulus convection. *Quart. J. Roy. Meteor. Soc.*, **130**, 3365–3383.
- Stone, D. A., and A. J. Weaver, 2003: Factors contributing to diurnal temperature range trends in twentieth and twenty-first century simulations of the CCCma coupled model. *Climate Dyn.*, **20**, 435–445.
- Stull, R. B., 1984: Transient turbulence theory. Part I: The concept of eddy-mixing across finite distances. *J. Atmos. Sci.*, **41**, 3351–3367.
- Suarez, M. J., A. Arakawa, and D. A. Randall, 1983: The parameterization of the planetary boundary layer in the UCLA general circulation model: Formulation and results. *Mon. Wea. Rev.*, **111**, 2224–2243.
- Tiedtke, M., 1989: A comprehensive mass flux scheme for cumulus parameterization in large-scale models. *Mon. Wea. Rev.*, **117**, 1779–1800.
- Troen, I., and L. Mahrt, 1986: A simple model of the atmospheric boundary layer: Sensitivity to surface evaporation. *Bound.-Layer Meteor.*, **37**, 129–148.
- Van Leer, B., 1977: Towards the ultimate conservative difference scheme: IV. A new approach to numerical convection. *J. Comput. Phys.*, **23**, 276–299.
- Vogelezang, D. H. P., and A. A. M. Holtzlag, 1996: Evaluation and model impacts of alternative boundary-layer height formulations. *Bound.-Layer Meteor.*, **81**, 245–269.
- Wang, S., and B. A. Albrecht, 1990: A mean-gradient model of the dry convective boundary layer. *J. Atmos. Sci.*, **47**, 126–138.